The effect of detector nonlinearity on WFIRST PSF profiles for weak gravitational lensing measurements

A. A. Plazas[†a], C. Shapiro[a,b], J. Rhodes[a,b,c], & R. Smith[b]

[†]andres.a.plazas.malagon@jpl.nasa.gov

[a]Jet Propulsion Laboratory, California Institute of Technology, 4800 Oak Grove Dr., Pasadena, CA 91109, USA

[b]California Institute of Technology, 1200 E. California Blvd, CA 91125, USA

[c]Institute for the Physics and Mathematics of the Universe, 5-1-5 Kashiwanoha, Kashiwa, Chiba Prefecture 277-8583, Japan

ABSTRACT

Weak gravitational lensing (WL) is one of the most powerful techniques to learn about the dark sector of the universe. To extract the WL signal from astronomical observations, observed galaxy shapes must be measured and corrected for the Point Spread Function (PSF) of the imaging system with extreme accuracy (of the order of 1 part per 1000 in the fractional and absolute errors in size and ellipticity). Biases in shape measurements can potentially originate in the detectors by any particular instrument. Future missions such as NASA's Wide Field Infrared Survey Telescope-Astrophysics Focused Telescope Asset (WFIRST) will use a new family of hybrid near-infrared CMOS detectors (HAWAII-4RG) that are untested for accurate WL measurements. Like any other detector, these devices are intrinsically subject to non-linearities in the conversion of photo-generated charge to measured voltage that tend to attenuate bright objects such as reference stars that are used for PSF determination. In this paper, we study and set preliminary requirements on the impact on WFIRST PSF properties (size and ellipticity) induced by this type of detector non-linearity (NL), setting preliminary requirements We use the publicly-available `GalSim` and the WFIRST Exposure Time Calculator codes to generate customized simulations of the PSF optical profiles expected for WFIRST and study the consequences of a one-parameter non-linearity function quadratic in the signal Q (in electrons) per pixel, $f(Q) = Q - \beta Q^2$. We use these simulations to measure the fractional error in the PSF size ($\Delta R/R$) and the absolute error in the PSF ellipticity (Δe) as a function of parameters such as the expected magnitude of typical stars in WFIRST and β. For a nominal $\beta_0 = 3.566 \times 10^{-7}/e^-$, NL attenuates the signal by $\sim 4\%$ for a pixel full well depth of about 1.1^5 e^-. Since the NL effects depend on PSF size and flux, we find variation in its amplitude among the four bands of the High Latitude Survey (HLS) of WFIRST (being the largest for the J129 band). As β is allowed to increase, the values of $\Delta R/R$ and Δe increase linearly in all bands

at a fixed magnitude. Uncalibrated, NL at its nominal value can induce an error of $\Delta R/R = 2.5 \times 10^{-3}$ and $\Delta e_2 = 5\times^{-4}$ in the WFIRST PSF size and ellipticity in the H158 bandpass for the expected brightest stars (AB magnitude of $\sim m = 20$) in the HLS of WFIRST. In addition, our simulations show that to limit the bias of $\Delta R/R$ and Δe in the H158 band to better than 1 part in 1000, the mean β must be calibrated to $\sim 3.5\%$ and $\sim 10\%$, respectively.

1. Introduction

Weak gravitational lensing (WL) has been identified as a powerful probe of the nature and evolution of the components of the Universe. In particular, *cosmic shear*-the subtle distortions of background galaxy shapes by the large scale structure of the Universe-constrains the properties of dark matter and dark energy through the measurement of the expansion history and growth of structure of the Universe (Réfrégier 2003; Hoekstra and Jain 2008; Kilbinger 2015). WL measurements also allow to test the validity of General Relativity that relates the gravitational potential to the matter-energy distribution. Several visible surveys of > 1000 deg^2 of the sky are currently underway and use the WL signal from hundreds of millions of galaxies as one of their central scientific techniques (*e.g.*, the Dark Energy Survey (DES) (Diehl and Dark Energy Survey Collaboration 2012; Jarvis et al. 2015), the the Kilo-Degree Survey (KiDS) (Kuijken et al. 2015), and the Hypersuprime-Camera Survey (HSC)(Miyazaki et al. 2012). In addition, future ground- and spaced-based surveys and missions in the visible and near infra-red (NIR) are planned to image more than $O(10^9)$ galaxies in the next decade (*e.g.*, the Large Synoptic Survey Telescope (LSST) (Ivezic et al. 2008), the Euclid spacecraft (Laureijs et al. 2011) and NASA's planned Wide Field Infrared Survey Telescope (WFIRST) in its Astrophysics Focused Telescope Asset (AFTA) implementation (Green et al. 2012; Spergel et al. 2013, 2015)).

The process of extracting the WL signal from images of the sky, in the presence of intrinsic galaxy ellipticity variations that are ~ 0.4 r.m.s, is highly non-trivial. It must be done through an statistical analysis of large galaxy samples, with a careful control of systematic uncertainties. The dominant signal produced by WL can be described by a local linear transformation of the source image that produces a shear (a complex, spin-2 field of components γ_1 and γ_2) and a scalar magnification, both of which have an r.m.s. amplitude of only $\sim 2\%$ in the case of cosmic shear. Most of the background galaxies usable by WL are at hight redshift (with low signal-to-noise (S/N) ratio) and with a size comparable or smaller than the Point Spread Function (PSF) of the imaging system. The PSF itself is usually larger than the lensing signal by an order of magnitude, inducing a modulation in the signal (multiplicative errors) and asymmetries that produce coherent spurious patterns (additive errors) that mimmic the WL signal. Bright stars are commonly used to estimate the PSF function, and then this information must be interpolated to the observed galaxy positions to deconvolve the PSF contribution and measure the galaxy shape (in the form of a complex

ellipticity $e = e_1 + ie_2$) to estimate the shear field[1]. This interpolation step is subject to introduce systematic errors if the information inferred from the stars does not fully constrain the PSF at the galaxy position with the required accuracy. In order not to bias the determination of cosmological parameters and dark energy, the ellipticity and size of the PSF must be known to an accuracy of $O(10^{-3})$ (Huterer et al. 2006; Amara and Réfrégier 2008; Paulin-Henriksson et al. 2008, 2009; Massey et al. 2013; Cropper et al. 2013) or better (4.7×10^{-4} for the knowledge of the WFIRST PSF ellipticity (Spergel et al. 2013)).

Systematic errors that originate from a telescope's detectors (image sensors) can introduce biases in astronomical observables such as photometry and astrometry that propagate into shear measurement biases. These type of errors have been extensively studied in the case of thick, fully-depleted, high-resistivity Charge Coupled-Devices (CCDs), which are the detectors of choice for many current and planned surveys such as DES, HSC, and LSST (Stubbs 2014; Plazas et al. 2014; Gruen et al. 2015). It is of great importance to qualitatively quantify the impact of these sensor effects on the inference of cosmological parameter, in particular through WL (Jarvis 2014; Mandelbaum 2015; Meyers and Burchat 2014). Future missions such as the James Webb Space Telescope and WFIRST will utilize a new family of near-infrared detectors that are subject as well to effects such as non-linearity, reciprocity failure (Bohlin et al. 2005; Biesiadzinski et al. 2011), interpixel capacitance (IPC) (McCullough 2008; Kannawadi et al. 2015), and persistence (Smith et al. 2008), and that can potentially imprint biases on weak lensing shape measurements if not taken into account.

In this paper we study the effect on PSF size and ellipticity of the non-linearity in the conversion of photo-generated charge to measured voltages in the NIR detectors that will be used by NASA's WFIRST mission. This type of detector non-linearity (NL) will tend to attenuate the measured flux in bright stars, broadening the inferred PSF and complicating its deconvolution from the observed galaxy image, which itself is fainter and less subject to the effects of NL. Our analysis is also useful to set preliminary requirements on NL for these sensors. We use the `python`/`C++` code `GalSim`[2] (Rowe et al. 2015) to create PSF profiles with the optical properties of WFIRST to analyze the impact of NL on PSF size and ellipticity.

In Section §2 we summarize the main characteristics of the NIR detectors that will be used in WFIRST and describe NL. In Section §3 we describe the simulations we create to study NL for WFIRST PSF profiles. Section §4 presents our main results on fractional errors in size and absolute errors in ellipticity caused by NL, as function of relevant parameters such as mean non-linearity amplitude and PSF magnitude. We conclude in Section §5 with a discussion of our results

---

[1]Most of the shape measurement algorithms to date rely on the accurate measurements of galaxy shapes to produce an estimator of the WL shear field (γ_1, γ_2). However, recent algorithms propose skipping this step and creating a direct shear estimator through Bayesian analysis in Fourier space (Bernstein and Armstrong 2014; Bernstein et al. 2015))

[2]`https://github.com/GalSim-developers`, `https://wfirst.ipac.caltech.edu/sims/Code.html`

and how they can be used in the derivation of NIR detector specifications to satisfy WL accuracy requirements.

2. Voltage non-linearity in the NIR detectors of WFIRST

The WFIRST mission will use a 2.4-m telescope equipped with a Wide Field Instrument (WFI) with 6 bandpass filters (Z087, Y106, J129, W149, H158, and F184 (Spergel et al. 2015)).[3] The WFI will perform a high-latitude survey (HLS) over an area of 2200 deg^2 in four NIR ($\sim 0.92 - 2.00\mu m$) bands (Y106, J129, H158, and F184) down to a 5σ point-source AB magnitude of 26.7 in J. The weak lensing program in the HLS will measure shapes of about 380 million galaxies in the J129, H158, and F184 (Green et al. 2012; Spergel et al. 2015)

The WFI possesses a wide-field channel that has a Focal Plane Assembly (FPA) of 18 4k×4k HgCdTe NIR detectors, arranged in a 6x3 layout and with a pixel size and plate scale of 10 μm and 0.11 arcseconds per pixel, respectively. The HgCdTe NIR detectors are manufactured by Teledyne Imaging Systems, and are part of a family of detectors known as HXRG[4].

The detector arrays are fabricated with a hybrid complementary metal-oxid-semiconductor (CMOS) architecture, which combines the qualities of HgCdTe to detect IR light (*e.g.*, altering the relative molar contributions of mercury and cadmium allows to tune the band gap up to an order of magnitude) and the advanced readout performance of integrated circuits. Light is absorbed, converted to charge through the photoelectric effect, and collected by electric fields generated by a reverse-biased p-n junction in the detector layer. The charge per pixel is then converted to a voltage and amplified through a source follower. This operation is performed in the silicon readout integrated circuit (ROIC) layer, which is connected to the HgCdTe detection layer by indium interconnects (one bump per pixel). Finally, the ROIC transfers the signal (and for this it is also known as "multiplexer") to the off-chip electronics at the edge of the FPA, where it is digitized through analog-to-digital converters (Beletic et al. 2008).

An ideal detector would produce a measurable signal that is proportional to the detected photons. However, there are several places in the signal chain where this expected linearity is not realized, and the conversion of charge to measured voltage (or analog-to-digital units, ADU) becomes non-linear. First of all, the charge accumulation rate might be a function of the photon-accumulation rate. This type of effect is known as reciprocity failure (RF), and it is a flux-dependent non-linearity (Smith et al. (2008), Biesiadzinski et al. (2011)). In addition to RF, the p-n junction acts as a parallel-plate capacitor, and as charge accumulates the depletion region narrows, causing a deviation from linearity of the charge-to-voltage conversion relation. Non-linearity can also be

---

[3]In addition to a integral field unit and a coronagraph for supernovae and exoplanet studies, respectively

[4]"HAWAII Xk×Xk pixels with Reference pixels and Guide mode", where "HAWAII" stands for HgCdTe Astronomical Wide Area Infrared Imager

introduced through the electronic gain of the ROIC.

The last two types of non-linearity depend on fluence (total flux per pixel, or integrated signal, as opposed to RF, which is flux dependent), and can be analyzed together in a singe transfer function typically called "nonlinearity". We study the impacts of NL (more relevant at high signals) on PSF measurements in this paper, while we leave investigations on the consequences of RF (relevant at lower signals) on WL measurements for future work.

Measurements with H2RG 1.7μm cutoff detectors produced for the NIR channel of the Wide Field Camera 3 (WFC3) installed onboard the Hubble Space Telescope (with the same basic design of the H4RG that will be used in the WFI but with 18 μm pixels) show that the voltage relation for a measured signal S is well fit by a quadratic function in the *mean* signal $\langle Q \rangle$ of the form:

$$S(\langle Q \rangle) = \langle Q \rangle - \beta \langle Q \rangle^2 \ \ (e^-) \tag{1}$$

We *assume* that each individual pixel satisfies a NL function of the same form as Eq. 1, and that the spatial variation on NL is such as the non-linearity coefficient β in each pixel can be drawn from a Normal distribution of the form $\mathcal{N} \sim (\beta_0, 0.12\beta_0)$, where the nominal value $\beta_0 \equiv 3.566 \times 10^{-7}/e^-$ and the dispersion parameter of the distribution (r.m.s.= $0.12\beta_0$) includes shot noise and deviations of the individual NL curves from the mean NL. This mean nominal value implies an attenuation of the signal of about 4% for a pixel full well depth in the WFI detectors of 1.1×10^5 electrons [5] (Eq. 1). We assume that galaxies will have about two orders of magnitude less total electrons than bright stars, and therefore for this quadratic model, star shapes are distorted by NL and galaxies are (approximately) not, which would result in incorrect PSF correction if not accurately calibrated. We have verified that the results using the mean NL coefficient for all pixels do not differ significatively from those using the distribution above for each pixel.

We apply this mapping to simulated WFIRST PSF profiles and quantify the impact on PSF properties such as size and shape.

3. Methods

3.1. Simulations

We use the publicly available `GalSim` code (v.13) to simulate the impact of NL on the WFIRST PSF shape and size. `GalSim` is a `python/C++` open-source code that allows the user to create simulations of astronomical objects, and it is especially useful in weak lensing investigations.

Kannawadi et al. (2015) have developed within `GalSim` (v1.3) a WFIRST module called "`galsim.wfirst`", which allows the simulation of a PSF profile according to the optical design char-

---

[5]Dave Content (GSFC), private communication.

acteristics of the WFIRST WFI (Pasquale et al. 2014))[6]) through the calling of `galsim.wfirst.getPSF` routine. This routine returns a `python` dictionary of `galsim.ChromaticOpticalPSF` objects indexed by each one of the 18 H4RG detectors of the FPA. It uses the optical configuration of the pupil plane to simulate PSF images in any WFIRST WFI bandpass filter, with expected optical aberrations approximated as a linear combination of Zernike polynomials (up to Noll order equal to 11, Noll (1976)). For this work, we have created simulations in four bands of the HLS (see Table 1). A central circular obscuration (30%) and six support struts are included as well. The pupil plane configurations and Zernike models are publicly available.[7]

The current version of the module does not include PSF variations across the detector field of view, and the PSF returned corresponds to that at its center. In addition, the module assumes that the pupil plane configuration of all the six bands is the same and equivalent to that of the "red" bands (*i.e.*, W149, H158, and F184), and that the struts are not, in general, radial nor evenly spaced. However, these last two assumptions can be relaxed to expedite calculations, and the optional keyword `approximate_struts` can be set to `True`. The module generates PSF models that do not include pointing jitter nor charge diffusion. These effects could be added to the profile (*e.g.,* by means of an extra convolution with a Gaussian profile in the case of diffusion), but we did not include them in our simulations. Their effect would be to create a slightly larger PSF, reducing the impact NL. Their omission makes our results slightly conservative.

To make our results conservative, we simulate only detector #18, whose PSF was determined to have the largest ellipticity (see below for a description of the shape measurement method used) across all bands among all the detectors (Table 1). Aberrations such as defocus, astigmatism, coma, and line-of-sight motion patters couple to propagate into terms that produce azimuthally asymmetrical profiles. We also evaluate the PSF at the mean wavelength weighted by each bandpass or effective wavelength, and set the `approximate_struts` keyword to `False` when creating the profile. We then form an effective PSF by convolving the profile with a 2D box car profile of length equal to the nominal plate scale of the WFIRST WFI (`galsim.wfirst.pixel_scale`= 0.11 arcseconds per pixel).

The resulting PSF profile created in this way will be undersampled (in accordance with the WFIRST WFI design). In order to maximize the field of view, detectors in instruments of space missions are usually built with a physical size that results in undersampled images, which fail to satisfy the Nyquist-Shannon criterium for the maximum band limit set by the optical response of the system, and therefore produce aliased images.[8] In general, it is not possible to recover all the information of a continuous function from a discrete sample of points if the image is aliased, and

---

[6]Pasquale et al. (2014) discuss the so-called "Cycle 4" optical design, whereas the `GalSim` WFIRST module -used in this work- uses files corresponding to "Cycle 5"

[7]`http://wfirst.gsfc.nasa.gov/science/sdt_public/wps/references/instrument/`

[8]The Nyquist-Shannon criterium states that the sampling interval p must satisfy $p < 1/(2u_{max})$, where u_{max} is the highest frequency in the signal, in order to avoid aliasing.

Band	Min. λ (μm)	Max. λ (μm)	λ_{eff} (μm)	$k(\lambda)$ (e^-)	e_1 (chip #18)	e_2 (chip #18)	σ (pix) (chip #18)
Y106	0.900	1.010	0.873	3.4470×10^4	0.00841	0.2010	4.4455
J129	1.095	1.500	1.292	9.5477×10^4	0.00793	0.1313	4.5140
H158	1.340	1.830	1.577	9.5178×10^4	0.00790	0.0807	4.8340
F184	1.630	2.060	1.837	7.1792×10^4	0.00592	0.0557	5.2781

Table 1: The first column lists the four bands that will be used in the HLS. For weak lensing analysis, multi-band shape measurement will be done in J129, H158, and F184. Columns 2, 3, and 4 show their minimum, maximum, and effective wavelengths, respectively (from Kannawadi et al. (2015)). Column 5 shows the baseline flux (in electrons) $k(\lambda)$ of Eq. 3 at AB magnitude 20 as calculated by the ETC-WL, using the parameters defined in the Appendix. The last three columns show the ellipticity components and size of the WFIRST PSF profile in detector number 18 as calculated by the adaptive moments routine in `GalSim`. chip 18 was found to possess the largest values of absolute PSF ellipticity.

measurements of astronomical object's properties such as magnitude and shape will be erroneous (Lauer 1999a; Fruchter 2011; Rhodes et al. 2007). Also, in particular, we found that our shape measurement algorithm fails when most light is concentrated in a few pixels.

To overcome this problem in real data, multiple dithered exposures are taken, and then put together by means of an image combination algorithm(Lauer 1999b; Fruchter and Hook 2002; Bertin 2006; Rowe et al. 2011) in order to produce an oversampled image that satisfies the Nyquist-Shannon criterium. To study NL with simulations, however, we do not make use of such external software—which can be computationally expensive—to produce an image at higher resolution. Instead, we have used an approximation where we draw `GalSim`objects at a high resolution through the method `galsim.GSObject.drawImage`[9], setting the parameter `scale` to p/N, where $N \in \mathbb{Z}^+$ and p is the native pixel scale. We apply the effect of NL to the convolved PSF profile, including the pixel response at its native scale, and then render it with a resolution p/N. Defining $Q \equiv 1/p \times u_{\text{max}}$ as the sampling factor ($Q < 2$, $Q = 2$, and $Q \geq 2$ represent under-, critically, and over-sampled images, respectively), we see that in order to produce an over-sampled image ($Q \geq 2$), the Nyquist-Shannon criterium implies that N must be given by (see *e.g.*, Marks (2009); Shapiro et al. (2013))

$$N = \frac{2p}{\lambda_{min} F} \tag{2}$$

where p is the pixel size, λ_{min} is the shortest wavelength in a given filter, and F is the the f-number of the telescope. In the case of the WFIRST telescope, $p = 10$ μm and $F = 7.8$, resulting in $N \geq 3$ ($N \geq 2$) for the J129 (H158) band. However, we have conservatively chosen a larger N for

---

[9]The keyword `method` should be set to '`no_pixel`' when calling `galsim.GSObject.drawImage`, since by default it convolves its argument profile with a boxcar of length `pixel_scale`. This extra convolution must be turned off because the effective PSF profile we create already includes this pixel response.

our simulations to reduce discretization errors. We have verified the convergence of our results for $N \geq 6$.

Notice that this method to approximate oversampled images can only be used in the case of sensor effects such as NL, which only depend on each pixel individually. In the case of other effects that correlate the signal in one pixel with the signal of its neighbors (such as IPC), the effect should be applied to the native scale of the detector and then a properly sampled image should be generated through appropriate combination of several dithered images before performing any analysis (see for instance the "interleaving" algorithm of Kannawadi et al. (2015), also included in `GalSim`).

The PSF profiles are drawn into square postage stamps of size 1.5k pixels (k=1024), large enough to ensure that most of the flux applied to the original profile object is conserved when drawing the image. Each profile object was assigned a total flux of

$$f = k(\lambda) \times 2.521^{(20-m)} \ e^-, \tag{3}$$

which is the number of source counts per exposure and where m represents the AB magnitude of the object. $k(\lambda) \ e^-$ is a baseline flux at AB magnitude $m = 20$ determined by using the WFIRST Exposure Time Calculator[10] (Hirata et al. 2012) in weak lensing mode (ETC-WL). Notice that in our simulations we have neglected the main sources of noise that would affect the HLS (zodiacal background, thermal emission, dark current, and read noise), which would make all images slightly more nonlinear.

Among other parameters, the flux depends on each bandpass filter, and its values are listed in 1 for the particular set of parameters of the listed in the Appendix. The brightest magnitude used was AB $m = 20$, based on the number of source counts in the J129 band calculated by the ETC-WL ($\sim 9.5477 \times 10^4$ electrons, representing about 86% of the typical full well depth of the H4RG detectors of $\sim 1.1 \times 10^5$ electrons). However, since NL is a function of signal, the total flux in the higher resolution image must be multiplied by a factor of N^2 to preserve the appropriate response per pixel to this effect, correcting for the fact that the new image has a factor of N^2 more pixels than the one created at the native scale.

For simplicity of analysis, the postage stamps are noiseless and no other sensor effect is applied. NL is then (after convolving with a pixel of the size of the native scale) by using Eq. 1 through the use of the `galsim.image.applyNonlinearity` method.

Fig. 1 shows an example of the PSF profiles and postage stamps created for our simulations (J129 band). The effect of NL (at the nominal β_0) is small, and the difference image reveals that the attenuation in the flux is of the order of a few percent, mainly for the larger signals found at the core of the PSF. Kannawadi et al. (2015) present more details on the `galsim.wfirst` module, along with examples of the profiles that can be generated in all 6 WFIRST filters.

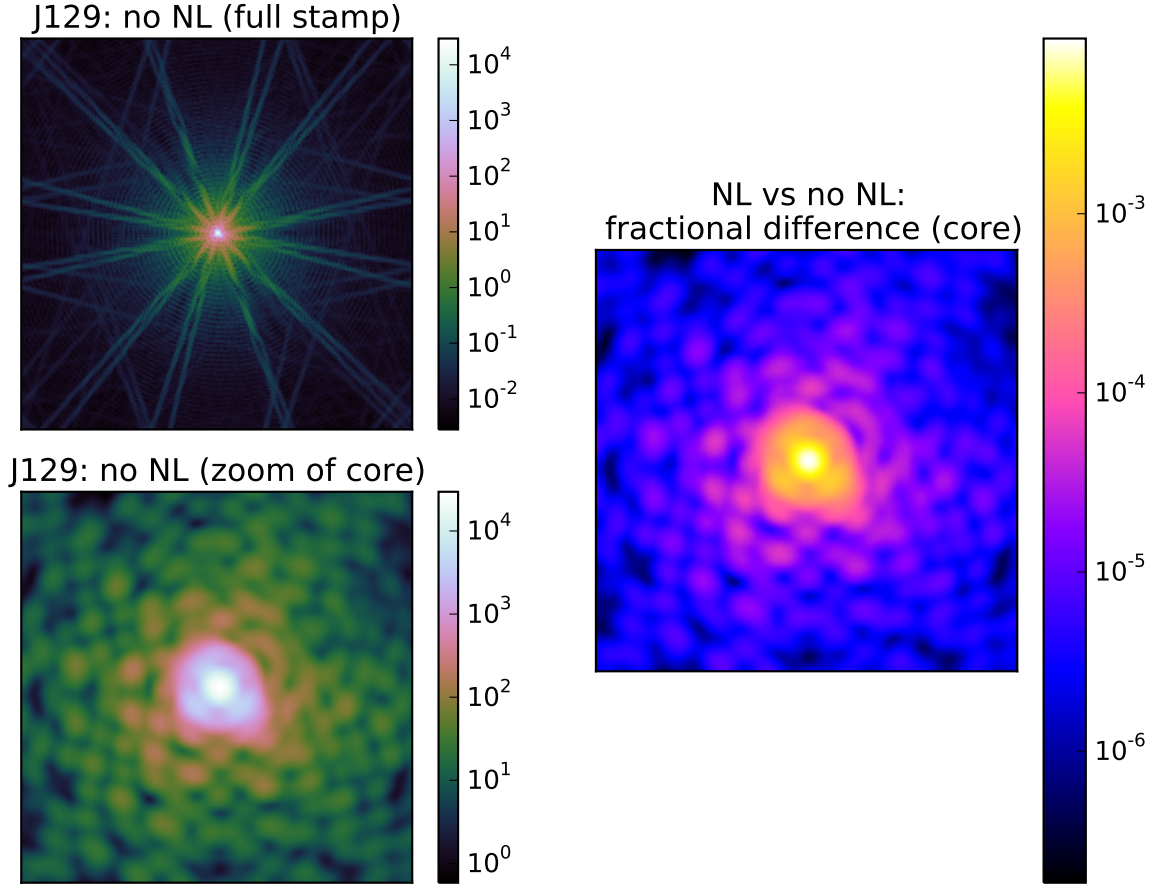[10]`https://wfirst.ipac.caltech.edu/sims/tools/wfDepc/wfDepc.html`

Fig. 1.— Example of the WFIRST PSF profiles in the J129 band created by the `galsim.wfirst.getPSF` method. Each postage stamp has a size of 1.5×1.5k pixels ($k = 1024$), and is drawn at a resolution of p/N, with $p = 0.11$ arcseconds and $N = 6$. Before drawing the profiles, they are first convolved with a pixel response of size p and given a flux according to the ETC-WL (with the parameters of the Appendix) at an AB magnitude of 20 (9.5477×10^4 e^{-1}, Table 1). However, to preserve the right response to NL, the higher-resolution image has N^2 more total flux. The NL effect is applied at the native pixel scale p. Diffraction spikes and structures can be seen due to the optical properties and aberrations of the PSF model used (upper left panel). The upper left panel shows the full postage stamp PSF image without the NL applied, while the lower left panel shows a zoom in to the core. The fractional difference between the PSF without the NL applied and a PSF with NL using a nominal $\beta_0 = 3.566 \times 10^{-7}/e^-$ is of the order of 1% in the core pixels which have more flux, and it is better seen in the right-hand side image.

3.2. PSF size and shape measurement

The accurate determination of PSF properties such as size and ellipticity is crucial to avoid the propagation of systematic biases in cosmological parameters through the use of weak gravitational lensing (Paulin-Henriksson et al. 2008, 2009; Massey et al. 2013; Cropper et al. 2013). In general, the problem of galaxy and PSF shape measurements for accurate weak lensing is non-trivial, and even when the PSF is perfectly known, shape measurement algorithms can introduce biases. Several shape measurements algorithms–ranging from model-fitting methods to particular combinations of weighted central moments–have been and are being investigated in order to produce accurate shear estimators that satisfy the requirements of current and future WL surveys (Mandelbaum et al. 2014).

To measure the profile shapes and size, we use the adaptive moments method (Bernstein and Jarvis 2002; Hirata and Seljak 2003), which is already implemented in `GalSim` as `galsim.hsm.Find-AdaptiveMom()`. Adaptive moments are effectively weighted by an elliptical Gaussian. At first they are calculated by computing moments weighted by a circular Gaussian with some arbitrary size. Then the output moments are used to define a new elliptical Gaussian that will act as a new weight function. The process is iteratively repeated until the output moments are the same as those of the weight function. The ellipticity $e = e_1 + ie_2$ and size r are then defined as

$$e_1 = \frac{M_{xx} - M_{yy}}{M_{xx} + M_{yy}} \tag{4}$$

$$e_2 = \frac{2M_{xy}}{M_{xx} + M_{yy}} \tag{5}$$

$$r = \det[\mathbf{M}]^{1/4} \tag{6}$$

where the centroid $\bar{\mathbf{x}}$ and moment matrix $\mathbf{M}$ of an image are defined as

$$\bar{\mathbf{x}} = \frac{\int d^2\mathbf{x} \; w(\mathbf{x})\mathbf{x}I(\mathbf{x})}{\int d^2\mathbf{x} \; w(\mathbf{x})I(\mathbf{x})} \tag{7}$$

$$M_{ij} = \frac{\int d^2\mathbf{x} \; (\mathbf{x} - \bar{\mathbf{x}})_i(\mathbf{x} - \bar{\mathbf{x}})_j w(\mathbf{x})I(\mathbf{x})}{\int d^2\mathbf{x} \; w(\mathbf{x})I(\mathbf{x})} \tag{8}$$

for an elliptical Gaussian weight function $w(\mathbf{x})$.

3.3. Changes in size and ellipticity induced by NL

We quantify the effect of voltage non-linearity by measuring the fractional change in size and the absolute change in ellipticity of the PSF profiles, in the 4 filters of the HLS of WFIRST and for several values of the NL parameter β. We calculate the quantities Δe_1, Δe_2, and $\frac{\Delta R}{R}$, which are defined as the difference between the measured ellipticity or size after the effect (NL) is applied and the reference values measured before (represented by the subscript "0") the application of NL:

$$\Delta e_i \equiv e_i - e_{i,0}, \quad i \in [1, 2] \tag{9}$$

$$\frac{\Delta R}{R} \equiv \frac{R - R_0}{R_0} \tag{10}$$

In this way, we minimize the details and possible biased induced by the shape measurement algorithm, and concentrate only on the relative changes induced by the detector anomalies.

The basic process is summarized by the following steps:

1. Create a WFIRST PSF surface brightness profile with a given flux as prescribed by Eq. 3.

2. Convolve the PSF profile with a squared pixel response with the size of the native plate scale of the WFIRST FPA ($p = 0.11$ arcseconds per pixel) to produce an effective PSF.

3. Draw the effective PSF profile in a noiseless postage stamp of size $1.5k$ by $1.5k$ pixels ($k = 1024$) pixels at a higher resolution of of p/N, with $N = 6$, and multiply the resulting image by N^2. In this step, NL is not yet applied, but it will be done so in a later step, so the flux still needs to be adjusted.

4. Use the adaptive moments algorithm to measure the shape $e = (e_{1,0}, e_{2,})$ and size R_0 of the profile to have as baseline reference.

5. Create another image of the effective PSF at a higher resolution and with the flux adjusted as in 3. To apply NL, draw a β from the distribution $\mathcal{N} \sim (\beta_0, 0.12\beta_0)$ for each pixel in the high-resolution image I, and apply the voltage non-linearity to the postage stamps according to the transformation $I \mapsto I - \beta I^2$ (c.f. Eq. 1.)

6. Measure the shape and size of the object with the sensor effect applied, and calculate the quantities Δe_1, Δe_2, and $\frac{\Delta R}{R}$, as defined in Eqs. 9 and 10.

7. Repeat steps 5 and 6 for M realizations of the β distribution, and calculate the mean value of Eqs. 9 and 10 over all M realizations. The error bars will be given by the standard error of the mean. In our simulations, we use $M = 10$.

8. Repeat steps 1 to 7 for different AB magnitudes (fluxes) at fixed mean β and for different NL parameters at a fixed magnitude.

4. Results

Fig. 2 shows the fractional change in PSF size and the absolute error in PSF ellipticity as a function of the nonlinearity parameter β, for different bandpass filters at fixed AB magnitude of 20, consistent with the magnitude of brightest stars that will be usable for the HLS. The effect depends on flux, and hence its amplitude is the largest in the J129 bandpass filter (c.f., Table 1). In this band, the nominal value of $\beta_0 = 3.566 \times 10^{-7}/e^-$ induces errors in the size and ellipticity of about 5×10^{-3} and 8×10^{-4} respectively, comparable or even larger than the required values of 10^{-3} and
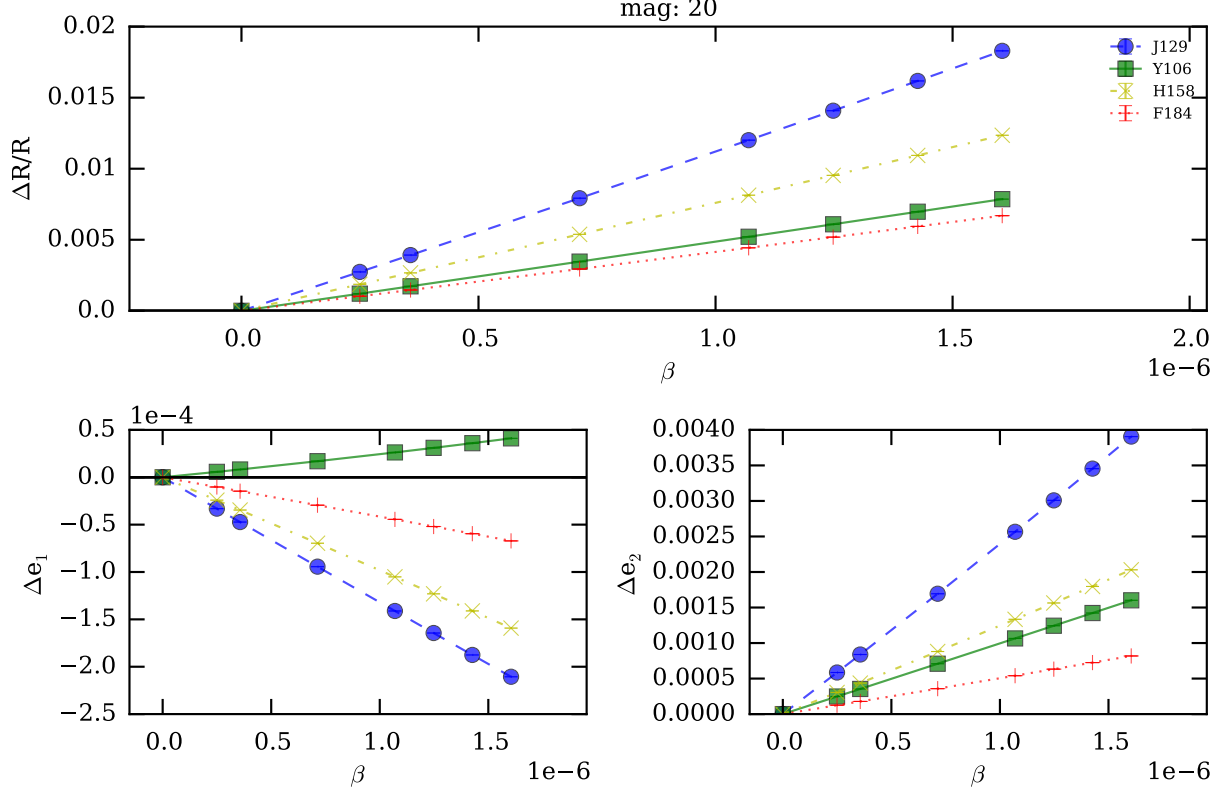
Fig. 2.— Fractional error in PSF size (upper panel) and absolute error in PSF ellipticity components (lower panels) as a function of nonlinearity parameter β for the WFIRST PSF, in four the four HSL filters (J129, Y106, H158, and F184), and an AB magnitude of 20 (similar plots were found for other values of magnitude). In each plot, the nominal value for the nonlinearity parameter as given by laboratory measurements, β_0, is located at the third point from the origin. Each point is the mean over $M = 10$ realizations of the parameter β per pixel, and the associated error bars (too small to be seen in the cases of $\Delta R/R$ and Δe_2) represent the standard error of the mean.

4.5×10^{-4} on the knowledge of the size and ellipticity of the PSF in order not to bias cosmological parameter inferences from WL experiments (Section §1). As the β parameter is increased, the amplitude of the errors increases approximately in a linear manner within the domain of β vales considered.

Since $\Delta R/R$ and Δe are approximately linear in β, we can condense this information by simply plotting the slope for various filters and star magnitudes.This is shown in Fig. 3, which shows $\Delta R/R/\beta$ and $\Delta e/\beta$ (the slopes in Fig. 2) vs m for each of the four filters of the HLS. From

Fig. 3, it is possible to estimate the precision to which β would have to be calibrated in order to limit the relative size and ellipticity bias of a star with a given magnitude. In particular, letting $(\beta - \beta_0)/\beta_0 \equiv \Delta\beta/\beta_0$ represent the fractional error in the measurement of a given value of β_0, we have:

$$\frac{\Delta R/R}{\Delta\beta} = c \quad \Rightarrow \quad \frac{\Delta R/R}{\Delta\beta/\beta_0} = c\beta_0 \quad \Rightarrow \quad \frac{\Delta\beta}{\beta_0} = \frac{\Delta R/R}{c\beta_0} \tag{11}$$

In Eq.11, c represents the ordinate value in Fig. 3 for a given magnitude, and we have replaced $\Delta R/R/\beta$ by $\Delta R/R/\Delta\beta$ since the linearity in the bias in $\Delta R/R$ and Δe vs β for all magnitudes makes the choice of the expansion point of the Taylor expansion unimportant (*i.e.*, it does not matter if the expansion is around $\beta = 0$ or $\beta = \beta_0$). An analogous equation to Eq. 11 can be written for the error in the ellipticity if $\Delta R/R$ is replaced by Δe.

Under this conditions, Fig. 3 shows that to limit the bias of $\Delta R/R$ (Δe) in the H158 band to 10^{-4} (4.7×10^{-5}) [11], β must be calibrated to $\sim 3.5\%$ ($\sim 10\%$) (using $c \sim 8 \times 10^3 e^-$ at $m = 20$ from the upper panel of Fig. 3, $c \sim 1300$ at $m = 20$ from the lower right panel of the same figure, and $\beta_0 = 3.566 \times 10^{-7}/e^-$) for the brightest stars usable by the HLS. Notice that the numbers for the tolerable errors on the size and ellipticity of the PSF are estimates; however, Eq. 11 and Fig. 3 can now be used to derive WFIRST detector requirements once true PSF requirements are chosen.

5. Conclusion

We have used the WFIRST module in `GalSim` to study the impact on PSF measurement for weak lensing science due to the non-linearity in the conversion of charge to voltage in near-infrared hybrid CMOS detectors (such as those that will be used in the Wide Field Imager of the WFIRST mission). The PSF profiles created by `galsim.wfirst` posses several of the design characteristics of the expected PSF of the mission, such as optical aberrations and pixel scale. We have also used the WFIRST Exposure Time Calculator in Weak Lensing mode to assign the PSF profiles fluxes per pixel consistent with the expected brightness of the HLS.

Voltage non-linearity–as studied in this work–encompasses the linearity due to the shrinking of the depletion region at the p-n junction as charge accumulates, and the deviation from linearity originating in the multiplexer gain. It depends on the total integrated signal (fluence), and it is more dominant at high signals than other types of non-linearity such as reciprocity failure, which dominate at lower signals. As such, NL will tend to attenuate the bright stars that are usually used for PSF estimation, introducing errors when de-convolving the PSF at the interpolated galaxy positions.

---

[11]Ten percent of the estimated budget of 10^{-3} and 4.7×10^{-4} in the knowledge of the PSF size and ellipticity, *c.f.*, Section §1
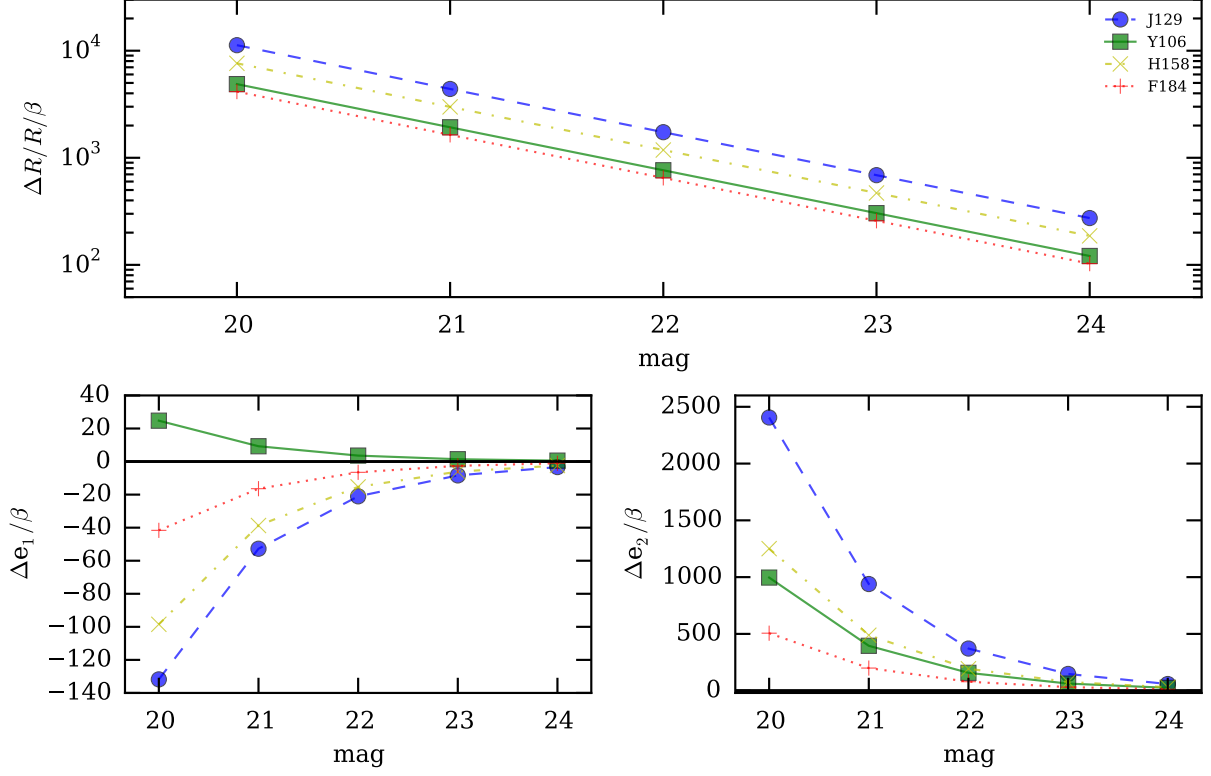
Fig. 3.— Fractional error in PSF size and absolute error in PSF ellipticity components normalized by the NL parameter β, as a function of magnitude for the four HSL filters (J129, Y106, H158, and F184). The ordinate axis in each plot represents the slope of the linear relationships in Fig. 2, derived by linear fitting of points around the vicinity of β_0 in each curve of that figure.

To model NL, we have used a single, one-parameter transfer function quadratic in the mean signal $\langle Q \rangle$ (Eq. 1). In principle, different pixels can have different underlying non-linearity coefficients which in practice can be difficult to measure with sufficient precision, so the mean response is usually measured. In our simulations, we have assumed that each individual pixel has a different non-linearity coefficient that follows a Normal distribution, and we have verified that the results obtained in this way do not differ from those obtained by using the mean NL coefficient for all pixels.

We have studied the impact of NL in isolation by using the relationship in Eq.1, not considering other sensor effects. We have used the metrics $\Delta R/R$ and Δe to assess the impact of NL on PSF size and ellipticity (which have to be controlled to $\sim O(10^{-3})$ or better), for different values of the

parameter space at hand (β, PSF magnitude, and bandpass filter to be utilized in WL analyses). In particular, our simulations show that the effects of NL are the largest in the J129 and linear with the nonlinearity parameter β. At the nominal value β_0, NL induces errors in PSF size and shape comparable to what is required by accurate WL measurements. For a particular set of estimated requirements on PSF size and ellipticity (10^{-4} and 4.7×10^{-5}, respectively), we find that the mean β should be calibrated to about 3–5%. However, the results derived in this study (Eq. 11 and Fig. 3) can be used to derive requirements on NL for the WFIRST detectors for a different set of tolerances on PSF properties.

We thank . . .

Appendix

The parameters used in the weak lensing mode of the Exposure Time Calculator (ETC-WL) to obtain the flux (in electrons) at AB magnitude 20 for each of the four bands simulated (J129, W149, H158, and F184) are as follows:

- telescope configuration: 0 (generic)

- aperture outer diameter: 2.4 m

- central obscuration: 0.3

- pixel scale: 0.11 arcsec/pix

- throughput: 0.8

- RMS wavefront error: 0.05 μm

- detector type: 2 (H4RG)

- pointing jitter: 0.00 arcsec per axis

- minimum wavelength: *filter dependent* (see Table 1)

- maximum wavelength: *filter dependent* (see Table 1)

- filter throughput: 0.99

- single exposure time: 174 s

- readnoise floor: 0.0 e$^-$/pix/s

- dark current: 0.0 e$^-$/pix/s

- (heliocentric) ecliptic latitude: -30 deg

- galactic redenning E(B-V): 0.03 mag

- number of exposures: 36 ($N = 6$)

- minimum resolution factor R: 0.425

- maximum ellipticity error: 0.2

REFERENCES

A. Amara and A. Réfrégier. Systematic bias in cosmic shear: extending the Fisher matrix. *MNRAS*, 391:228–236, November 2008. doi: 10.1111/j.1365-2966.2008.13880.x.

James W. Beletic, Richard Blank, David Gulbransen, Donald Lee, Markus Loose, Eric C. Piquette, Thomas Sprafke, William E. Tennant, Majid Zandian, and Joseph Zino. Teledyne imaging sensors: infrared imaging technologies for astronomy and civil space, 2008.

G. M. Bernstein and R. Armstrong. Bayesian lensing shear measurement. *MNRAS*, 438:1880–1893, February 2014. doi: 10.1093/mnras/stt2326.

G. M. Bernstein and M. Jarvis. Shapes and Shears, Stars and Smears: Optimal Measurements for Weak Lensing. *AJ*, 123:583–618, February 2002. doi: 10.1086/338085.

G. M. Bernstein, R. Armstrong, C. Krawiec, and M. C. March. An accurate and practical method for inference of weak gravitational lensing from galaxy images. *ArXiv e-prints*, August 2015.

E. Bertin. Automatic Astrometric and Photometric Calibration with SCAMP. In C. Gabriel, C. Arviset, D. Ponz, and S. Enrique, editors, *Astronomical Data Analysis Software and Systems XV*, volume 351 of *Astronomical Society of the Pacific Conference Series*, page 112, July 2006.

T. Biesiadzinski, W. Lorenzon, R. Newman, M. Schubnell, G. Tarlé, and C. Weaverdyck. Measurement of Reciprocity Failure in Near-Infrared Detectors. *PASP*, 123:179–186, February 2011. doi: 10.1086/658282.

R. C. Bohlin, D. J. Lindler, and A. Riess. Grism Sensitivities and Apparent Non-Linearity. Technical report, May 2005.

M. Cropper, H. Hoekstra, T. Kitching, R. Massey, J. Amiaux, L. Miller, Y. Mellier, J. Rhodes, B. Rowe, S. Pires, C. Saxton, and R. Scaramella. Defining a weak lensing experiment in space. *MNRAS*, 431:3103–3126, June 2013. doi: 10.1093/mnras/stt384.

T. Diehl and Dark Energy Survey Collaboration. The Dark Energy Survey Camera (DECam). *Physics Procedia*, 37:1332–1340, 2012. doi: 10.1016/j.phpro.2012.02.472.

A. S. Fruchter. A New Method for Band-limited Imaging with Undersampled Detectors. *PASP*, 123:497–502, April 2011. doi: 10.1086/659313.

A. S. Fruchter and R. N. Hook. Drizzle: A Method for the Linear Reconstruction of Undersampled Images. *PASP*, 114:144–152, February 2002. doi: 10.1086/338393.

J. Green, P. Schechter, C. Baltay, R. Bean, D. Bennett, R. Brown, C. Conselice, M. Donahue, X. Fan, B. S. Gaudi, C. Hirata, J. Kalirai, T. Lauer, B. Nichol, N. Padmanabhan, S. Perlmutter, B. Rauscher, J. Rhodes, T. Roellig, D. Stern, T. Sumi, A. Tanner, Y. Wang, D. Weinberg, E. Wright, N. Gehrels, R. Sambruna, W. Traub, J. Anderson, K. Cook, P. Garnavich, L. Hillenbrand, Z. Ivezic, E. Kerins, J. Lunine, P. McDonald, M. Penny, M. Phillips, G. Rieke, A. Riess, R. van der Marel, R. K. Barry, E. Cheng, D. Content, R. Cutri, R. Goullioud, K. Grady, G. Helou, C. Jackson, J. Kruk, M. Melton, C. Peddie, N. Rioux, and M. Seiffert.

Wide-Field InfraRed Survey Telescope (WFIRST) Final Report. *ArXiv e-prints*, August 2012.

D. Gruen, G. M. Bernstein, M. Jarvis, B. Rowe, V. Vikram, A. A. Plazas, and S. Seitz. Characterization and correction of charge-induced pixel shifts in DECam. *Journal of Instrumentation*, 10:C05032, May 2015. doi: 10.1088/1748-0221/10/05/C05032.

C. Hirata and U. Seljak. Shear calibration biases in weak-lensing surveys. *MNRAS*, 343:459–480, August 2003. doi: 10.1046/j.1365-8711.2003.06683.x.

C. M. Hirata, N. Gehrels, J.-P. Kneib, J. Kruk, J. Rhodes, Y. Wang, and J. Zoubian. The WFIRST Galaxy Survey Exposure Time Calculator. *ArXiv e-prints*, April 2012.

H. Hoekstra and B. Jain. Weak gravitational lensing and its cosmological applications. *Annual Review of Nuclear and Particle Systems*, 58:99–123, 2008.

D. Huterer, M. Takada, G. Bernstein, and B. Jain. Systematic errors in future weak-lensing surveys: requirements and prospects for self-calibration. *MNRAS*, 366:101–114, February 2006. doi: 10.1111/j.1365-2966.2005.09782.x.

Z. Ivezic, J. A. Tyson, B. Abel, E. Acosta, R. Allsman, Y. AlSayyad, S. F. Anderson, J. Andrew, R. Angel, G. Angeli, R. Ansari, P. Antilogus, K. T. Arndt, P. Astier, E. Aubourg, T. Axelrod, D. J. Bard, J. D. Barr, A. Barrau, J. G. Bartlett, B. J. Bauman, S. Beaumont, A. C. Becker, J. Becla, C. Beldica, S. Bellavia, G. Blanc, R. D. Blandford, J. S. Bloom, J. Bogart, K. Borne, J. F. Bosch, D. Boutigny, W. N. Brandt, M. E. Brown, J. S. Bullock, P. Burchat, D. L. Burke, G. Cagnoli, D. Calabrese, S. Chandrasekharan, S. Chesley, E. C. Cheu, J. Chiang, C. F. Claver, A. J. Connolly, K. H. Cook, A. Cooray, K. R. Covey, C. Cribbs, W. Cui, R. Cutri, G. Daubard, G. Daues, F. Delgado, S. Digel, P. Doherty, R. Dubois, G. P. Dubois-Felsmann, J. Durech, M. Eracleous, H. Ferguson, J. Frank, M. Freemon, E. Gangler, E. Gawiser, J. C. Geary, P. Gee, M. Geha, R. R. Gibson, D. K. Gilmore, T. Glanzman, I. Goodenow, W. J. Gressler, P. Gris, A. Guyonnet, P. A. Hascall, J. Haupt, F. Hernandez, C. Hogan, D. Huang, M. E. Huffer, W. R. Innes, S. H. Jacoby, B. Jain, J. Jee, J. G. Jernigan, D. Jevremovic, K. Johns, R. L. Jones, C. Juramy-Gilles, M. Juric, S. M. Kahn, J. S. Kalirai, N. Kallivayalil, B. Kalmbach, J. P. Kantor, M. M. Kasliwal, R. Kessler, D. Kirkby, L. Knox, I. Kotov, V. L. Krabbendam, S. Krughoff, P. Kubanek, J. Kuczewski, S. Kulkarni, R. Lambert, L. Le Guillou, D. Levine, M. Liang, K. Lim, C. Lintott, R. H. Lupton, A. Mahabal, P. Marshall, S. Marshall, M. May, R. McKercher, M. Migliore, M. Miller, D. J. Mills, D. G. Monet, M. Moniez, D. R. Neill, J. Nief, A. Nomerotski, M. Nordby, P. O'Connor, J. Oliver, S. S. Olivier, K. Olsen, S. Ortiz, R. E. Owen, R. Pain, J. R. Peterson, C. E. Petry, F. Pierfederici, S. Pietrowicz, R. Pike, P. A. Pinto, R. Plante, S. Plate, P. A. Price, M. Prouza, V. Radeka, J. Rajagopal, A. Rasmussen, N. Regnault, S. T. Ridgway, S. Ritz, W. Rosing, C. Roucelle, M. R. Rumore, S. Russo, A. Saha, B. Sassolas, T. L. Schalk, R. H. Schindler, D. P. Schneider, G. Schumacher, J. Sebag, G. H. Sembroski, L. G. Seppala, I. Shipsey, N. Silvestri, J. A.

Smith, R. C. Smith, M. A. Strauss, C. W. Stubbs, D. Sweeney, A. Szalay, P. Takacs, J. J. Thaler, R. Van Berg, D. Vanden Berk, K. Vetter, F. Virieux, B. Xin, L. Walkowicz, C. W. Walter, D. L. Wang, M. Warner, B. Willman, D. Wittman, S. C. Wolff, W. M. Wood-Vasey, P. Yoachim, H. Zhan, and for the LSST Collaboration. LSST: from Science Drivers to Reference Design and Anticipated Data Products. *ArXiv e-prints*, May 2008.

M Jarvis. Challenges for precision shape measurements. *Journal of Instrumentation*, 9(03):C03017, 2014. URL http://stacks.iop.org/1748-0221/9/i=03/a=C03017.

M. Jarvis, E. Sheldon, J. Zuntz, T. Kacprzak, S. L. Bridle, A. Amara, R. Armstrong, M. R. Becker, G. M. Bernstein, C. Bonnett, C. Chang, R. Das, J. P. Dietrich, A. Drlica-Wagner, T. F. Eifler, C. Gangkofner, D. Gruen, M. Hirsch, E. M. Huff, B. Jain, S. Kent, D. Kirk, N. MacCrann, P. Melchior, A. A. Plazas, A. Refregier, B. Rowe, E. S. Rykoff, S. Samuroff, C. Sánchez, E. Suchyta, M. A. Troxel, V. Vikram, T. Abbott, F. B. Abdalla, S. Allam, J. Annis, A. Benoit-Lévy, E. Bertin, D. Brooks, E. Buckley-Geer, D. L. Burke, D. Capozzi, A. Carnero Rosell, M. Carrasco Kind, J. Carretero, F. J. Castander, M. Crocce, C. E. Cunha, C. B. D'Andrea, L. N. da Costa, D. L. DePoy, S. Desai, H. T. Diehl, P. Doel, A. Fausti Neto, B. Flaugher, P. Fosalba, J. Frieman, E. Gaztanaga, D. W. Gerdes, R. A. Gruendl, G. Gutierrez, K. Honscheid, D. J. James, K. Kuehn, N. Kuropatkin, O. Lahav, T. S. Li, M. Lima, M. March, P. Martini, R. Miquel, J. J. Mohr, E. Neilsen, B. Nord, R. Ogando, K. Reil, A. K. Romer, A. Roodman, M. Sako, E. Sanchez, V. Scarpine, M. Schubnell, I. Sevilla-Noarbe, R. C. Smith, M. Soares-Santos, F. Sobreira, M. E. C. Swanson, G. Tarle, J. Thaler, D. Thomas, A. R. Walker, and R. H. Wechsler. The DES Science Verification Weak Lensing Shear Catalogs. *ArXiv e-prints*, July 2015.

A. Kannawadi, C. A. Shapiro, R. Mandelbaum, C. M. Hirata, J. W. Kruk, and J. D. Rhodes. The Impact of Interpixel Capacitance on WFIRST PSFs. *ArXiv e-prints*, December 2015.

M. Kilbinger. Cosmology with cosmic shear observations: a review. *Reports on Progress in Physics*, 78(8):086901, July 2015. doi: 10.1088/0034-4885/78/8/086901.

K. Kuijken, C. Heymans, H. Hildebrandt, R. Nakajima, T. Erben, J. T. A. de Jong, M. Viola, A. Choi, H. Hoekstra, L. Miller, E. van Uitert, A. Amon, C. Blake, M. Brouwer, A. Buddendiek, I. F. Conti, M. Eriksen, A. Grado, J. Harnois-Déraps, E. Helmich, R. Herbonnet, N. Irisarri, T. Kitching, D. Klaes, F. La Barbera, N. Napolitano, M. Radovich, P. Schneider, C. Sifón, G. Sikkema, P. Simon, A. Tudorica, E. Valentijn, G. Verdoes Kleijn, and L. van Waerbeke. Gravitational lensing analysis of the Kilo-Degree Survey. *MNRAS*, 454: 3500–3532, December 2015. doi: 10.1093/mnras/stv2140.

T. R. Lauer. The Photometry of Undersampled Point-Spread Functions. *PASP*, 111:1434–1443, November 1999a. doi: 10.1086/316460.

T. R. Lauer. Combining Undersampled Dithered Images. *PASP*, 111:227–237, February 1999b. doi: 10.1086/316319.

R. Laureijs, J. Amiaux, S. Arduini, J. . Auguères, J. Brinchmann, R. Cole, M. Cropper, C. Dabin, L. Duvet, A. Ealet, and et al. Euclid Definition Study Report. *ArXiv e-prints*, October 2011.

R. Mandelbaum. Instrumental systematics and weak gravitational lensing. *Journal of Instrumentation*, 10(05):C05017, 2015. URL `http://stacks.iop.org/1748-0221/10/i=05/a=C05017`.

R. Mandelbaum, B. Rowe, J. Bosch, C. Chang, F. Courbin, M. Gill, M. Jarvis, A. Kannawadi, T. Kacprzak, C. Lackner, A. Leauthaud, H. Miyatake, R. Nakajima, J. Rhodes, M. Simet, J. Zuntz, B. Armstrong, S. Bridle, J. Coupon, J. P. Dietrich, M. Gentile, C. Heymans, A. S. Jurling, S. M. Kent, D. Kirkby, D. Margala, R. Massey, P. Melchior, J. Peterson, A. Roodman, and T. Schrabback. The Third Gravitational Lensing Accuracy Testing (GREAT3) Challenge Handbook. *ApJS*, 212:5, May 2014. doi: 10.1088/0067-0049/212/1/5.

R. J. Marks. *Handbook of Fourier Analysis and Its Applications*. Oxford University Press, 1 edition, 2009.

R. Massey, H. Hoekstra, T. Kitching, J. Rhodes, M. Cropper, J. Amiaux, D. Harvey, Y. Mellier, M. Meneghetti, L. Miller, S. Paulin-Henriksson, S. Pires, R. Scaramella, and T. Schrabback. Origins of weak lensing systematics, and requirements on future instrumentation (or knowledge of instrumentation). *MNRAS*, 429:661–678, February 2013. doi: 10.1093/mnras/sts371.

P. McCullough. Inter-pixel capacitance: prospects for deconvolution. Technical report, August 2008.

J E Meyers and P R Burchat. Impact of chromatic effects on galaxy shape measurements. *Journal of Instrumentation*, 9(03):C03037, 2014. URL `http://stacks.iop.org/1748-0221/9/i=03/a=C03037`.

S. Miyazaki, Y. Komiyama, H. Nakaya, Y. Kamata, Y. Doi, T. Hamana, H. Karoji, H. Furusawa, S. Kawanomoto, T. Morokuma, Y. Ishizuka, K. Nariai, Y. Tanaka, F. Uraguchi, Y. Utsumi, Y. Obuchi, Y. Okura, M. Oguri, T. Takata, D. Tomono, T. Kurakami, K. Namikawa, T. Usuda, H. Yamanoi, T. Terai, H. Uekiyo, Y. Yamada, M. Koike, H. Aihara, Y. Fujimori, S. Mineo, H. Miyatake, N. Yasuda, J. Nishizawa, T. Saito, M. Tanaka, T. Uchida, N. Katayama, S.-Y. Wang, H.-Y. Chen, R. Lupton, C. Loomis, S. Bickerton, P. Price, J. Gunn, H. Suzuki, Y. Miyazaki, M. Muramatsu, K. Yamamoto, M. Endo, Y. Ezaki, N. Itoh, Y. Miwa, H. Yokota, T. Matsuda, R. Ebinuma, and K. Takeshi. Hyper Suprime-Cam. In *Society of Photo-Optical Instrumentation Engineers (SPIE) Conference Series*, volume 8446 of *Society of Photo-Optical Instrumentation Engineers (SPIE) Conference Series*, page 0, September 2012. doi: 10.1117/12.926844.

R. J. Noll. Zernike polynomials and atmospheric turbulence. *Journal of the Optical Society of America (1917-1983)*, 66:207–211, March 1976.

Jeffrey Kruk David Vaughnn Qian Gong Joseph Howard Alden Jurling Len Seals Eric Mentzell Nerses Armani Gary Kuan Pasquale et al., David Content. Optical design of the wfirst-afta wide-field instrument. *Proc. SPIE 9293, International Optical Design Conference 2014*, 2014.

S. Paulin-Henriksson, A. Amara, L. Voigt, A. Refregier, and S. L. Bridle. Point spread function calibration requirements for dark energy from cosmic shear. *A&A*, 484:67–77, June 2008. doi: 10.1051/0004-6361:20079150.

S. Paulin-Henriksson, A. Refregier, and A. Amara. Optimal point spread function modeling for weak lensing: complexity and sparsity. *A&A*, 500:647–655, June 2009. doi: 10.1051/0004-6361/200811061.

A. A. Plazas, G. M. Bernstein, and E. S. Sheldon. On-Sky Measurements of the Transverse Electric Fields' Effects in the Dark Energy Camera CCDs. *PASP*, 126:750–760, September 2014. doi: 10.1086/677682.

A. Réfrégier. Weak gravitational lensing by large-scale structure. *Annual Review of Astronomy and Astrophysics*, 41:645–668, 2003.

J. D. Rhodes, R. J. Massey, J. Albert, N. Collins, R. S. Ellis, C. Heymans, J. P. Gardner, J.-P. Kneib, A. Koekemoer, A. Leauthaud, Y. Mellier, A. Refregier, J. E. Taylor, and L. Van Waerbeke. The Stability of the Point-Spread Function of the Advanced Camera for Surveys on the Hubble Space Telescope and Implications for Weak Gravitational Lensing. *ApJS*, 172:203–218, September 2007. doi: 10.1086/516592.

B. Rowe, C. Hirata, and J. Rhodes. Optimal Linear Image Combination. *ApJ*, 741:46, November 2011. doi: 10.1088/0004-637X/741/1/46.

B. T. P. Rowe, M. Jarvis, R. Mandelbaum, G. M. Bernstein, J. Bosch, M. Simet, J. E. Meyers, T. Kacprzak, R. Nakajima, J. Zuntz, H. Miyatake, J. P. Dietrich, R. Armstrong, P. Melchior, and M. S. S. Gill. GALSIM: The modular galaxy image simulation toolkit. *Astronomy and Computing*, 10:121–150, April 2015. doi: 10.1016/j.ascom.2015.02.002.

C. Shapiro, B. T. P. Rowe, T. Goodsall, C. Hirata, J. Fucik, J. Rhodes, S. Seshadri, and R. Smith. Weak Gravitational Lensing Systematics from Image Combination. *PASP*, 125:1496–1513, December 2013. doi: 10.1086/674415.

R. M. Smith, M. Zavodny, G. Rahmer, and M. Bonati. A theory for image persistence in HgCdTe photodiodes. In *Society of Photo-Optical Instrumentation Engineers (SPIE) Conference Series*, volume 7021 of *Society of Photo-Optical Instrumentation Engineers (SPIE) Conference Series*, page 0, July 2008. doi: 10.1117/12.789372.

D. Spergel, N. Gehrels, J. Breckinridge, M. Donahue, A. Dressler, B. S. Gaudi, T. Greene, O. Guyon, C. Hirata, J. Kalirai, N. J. Kasdin, W. Moos, S. Perlmutter, M. Postman, B. Rauscher,

J. Rhodes, Y. Wang, D. Weinberg, J. Centrella, W. Traub, C. Baltay, J. Colbert, D. Bennett, A. Kiessling, B. Macintosh, J. Merten, M. Mortonson, M. Penny, E. Rozo, D. Savransky, K. Stapelfeldt, Y. Zu, C. Baker, E. Cheng, D. Content, J. Dooley, M. Foote, R. Goullioud, K. Grady, C. Jackson, J. Kruk, M. Levine, M. Melton, C. Peddie, J. Ruffa, and S. Shaklan. Wide-Field InfraRed Survey Telescope-Astrophysics Focused Telescope Assets WFIRST-AFTA Final Report. *ArXiv e-prints*, May 2013.

D. Spergel, N. Gehrels, C. Baltay, D. Bennett, J. Breckinridge, M. Donahue, A. Dressler, B. S. Gaudi, T. Greene, O. Guyon, C. Hirata, J. Kalirai, N. J. Kasdin, B. Macintosh, W. Moos, S. Perlmutter, M. Postman, B. Rauscher, J. Rhodes, Y. Wang, D. Weinberg, D. Benford, M. Hudson, W.-S. Jeong, Y. Mellier, W. Traub, T. Yamada, P. Capak, J. Colbert, D. Masters, M. Penny, D. Savransky, D. Stern, N. Zimmerman, R. Barry, L. Bartusek, K. Carpenter, E. Cheng, D. Content, F. Dekens, R. Demers, K. Grady, C. Jackson, G. Kuan, J. Kruk, M. Melton, B. Nemati, B. Parvin, I. Poberezhskiy, C. Peddie, J. Ruffa, J. K. Wallace, A. Whipple, E. Wollack, and F. Zhao. Wide-Field InfrarRed Survey Telescope-Astrophysics Focused Telescope Assets WFIRST-AFTA 2015 Report. *ArXiv e-prints*, March 2015.

C. W. Stubbs. Precision astronomy with imperfect fully depleted CCDs: an introduction and a suggested lexicon. *Journal of Instrumentation*, 9:C03032, March 2014. doi: 10.1088/1748-0221/9/03/C03032.